

Ossified blood vessels in primary familial brain calcification elicit a neurotoxic astrocyte response

Yvette Zarb,^{1,2} Ulrike Weber-Stadlbauer,³ Daniel Kirschenbaum,⁴ Diana Rita Kindler,⁵ Juliet Richetto,³ Daniel Keller,⁶ Rosa Rademakers,⁷ Dennis W. Dickson,⁷ Andreas Pasch,⁸ Tatiana Byzova,⁹ Khayrun Nahar,¹⁰ Fabian F. Voigt,^{2,11} Fritjof Helmchen,^{2,11} Andreas Boss,⁶ Adriano Aguzzi,⁴ Jan Klohs⁵ and Annika Keller^{1,2}

Brain calcifications are commonly detected in aged individuals and accompany numerous brain diseases, but their functional importance is not understood. In cases of primary familial brain calcification, an autosomally inherited neuropsychiatric disorder, the presence of bilateral brain calcifications in the absence of secondary causes of brain calcification is a diagnostic criterion. To date, mutations in five genes including solute carrier 20 member 2 (*SLC20A2*), xenotropic and polytropic retrovirus receptor 1 (*XPR1*), myogenesis regulating glycosidase (*MYORG*), platelet-derived growth factor B (*PDGFB*) and platelet-derived growth factor receptor β (*PDGFRB*), are considered causal. Previously, we have reported that mutations in *PDGFB* in humans are associated with primary familial brain calcification, and mice hypomorphic for *PDGFB* (*Pdgfb^{ret/ret}*) present with brain vessel calcifications in the deep regions of the brain that increase with age, mimicking the pathology observed in human mutation carriers. In this study, we characterize the cellular environment surrounding calcifications in *Pdgfb^{ret/ret}* animals and show that cells around vessel-associated calcifications express markers for osteoblasts, osteoclasts and osteocytes, and that bone matrix proteins are present in vessel-associated calcifications. Additionally, we also demonstrate the osteogenic environment around brain calcifications in genetically confirmed primary familial brain calcification cases. We show that calcifications cause oxidative stress in astrocytes and evoke expression of neurotoxic astrocyte markers. Similar to previously reported human primary familial brain calcification cases, we describe high interindividual variation in calcification load in *Pdgfb^{ret/ret}* animals, as assessed by *ex vivo* and *in vivo* quantification of calcifications. We also report that serum of *Pdgfb^{ret/ret}* animals does not differ in calcification propensity from control animals and that vessel calcification occurs only in the brains of *Pdgfb^{ret/ret}* animals. Notably, ossification of vessels and astrocytic neurotoxic response is associated with specific behavioural and cognitive alterations, some of which are associated with primary familial brain calcification in a subset of patients.

- 1 Department of Neurosurgery, Clinical Neuroscience Center, Zurich University Hospital, Zurich University, Zurich, Switzerland
- 2 Neuroscience Center Zurich (ZNZ), University of Zurich and ETH Zurich, Zurich, Switzerland
- 3 Institute of Veterinary Pharmacology and Toxicology, University of Zurich-Vetsuisse, Zurich University, Zurich, Switzerland
- 4 Institute of Neuropathology, Zurich University Hospital, Zurich University, Zurich, Switzerland
- 5 Department of Biomedical Engineering, ETH and University of Zurich, Zurich, Switzerland
- 6 Institute of Diagnostic and Interventional Radiology, Zurich University Hospital, Zurich University, Zurich, Switzerland
- 7 Department of Neuroscience, Mayo Clinic, Jacksonville, FL, USA
- 8 Calciscon AG, Nidau-Biel, Switzerland
- 9 Department of Molecular Cardiology, Lerner Research Institute, Cleveland Clinic, Cleveland, OH, USA
- 10 Department of Immunology, Genetics and Pathology, Uppsala University, Uppsala, Sweden
- 11 Brain Research Institute, Zurich University, Zurich, Switzerland

Received August 10, 2018. Revised December 7, 2018. Accepted December 26, 2018. Advance Access publication February 25, 2019

© The Author(s) (2019). Published by Oxford University Press on behalf of the Guarantors of Brain.

This is an Open Access article distributed under the terms of the Creative Commons Attribution Non-Commercial License (<http://creativecommons.org/licenses/by-nc/4.0/>), which permits non-commercial re-use, distribution, and reproduction in any medium, provided the original work is properly cited. For commercial re-use, please contact journals.permissions@oup.com

Correspondence to: Annika Keller
 Department of Neurosurgery, Clinical Neuroscience Center, Zurich University Hospital
 Zurich University, Zurich, Switzerland
 E-mail: Annika.Keller@usz.ch

Keywords: neurotoxic astrocyte; ossification; PDGFB; prepulse inhibition; primary familial brain calcification

Abbreviations: CEP = 2- ω -carboxyethylpyrrole; PFBC = primary familial brain calcification; PPI = prepulse inhibition; SWI = susceptibility-weighted imaging

Introduction

Brain calcification is the most common incidental finding seen in up to 20% of patients undergoing neuroimaging (Deng *et al.*, 2015). It is estimated that 30% of aged individuals present with brain calcifications (Nicolas *et al.*, 2013a). Intracranial vessel-associated calcifications have been reported to accompany neurodegenerative diseases (e.g. Alzheimer's, Parkinson's, Nasu-Hakola), type I interferonopathies, brain tumours and other disorders (Mann, 1988; Vermersch *et al.*, 1992; Volpi *et al.*, 2016). Functional contribution of cerebrovascular calcification to clinical manifestation of neurological diseases is debated (Puvanendran *et al.*, 1982; Forstl *et al.*, 1992); however, the occurrence of vascular calcifications in peripheral diseases (e.g. chronic kidney disease) can be detrimental (Zhu *et al.*, 2012). Moreover, although cerebrovascular calcifications are common, little is known about the mechanisms leading to their formation. Thus, there is a void in knowledge on the formation and functional consequences of cerebrovascular calcifications.

In the case of primary familial brain calcification (PFBC) the presence of calcifications in the brain is a diagnostic criterion. PFBC is a neuropsychiatric disease, in which all patients present with bilateral, vessel-associated calcifications in the basal ganglia (Norman and Urich, 1960; Gomez *et al.*, 1989) in the absence of other secondary causes of brain calcification (e.g. imbalance in serum calcium and phosphate levels) (Manyam, 2005). Dominantly-inherited PFBC is associated with mutations in four genes: solute carrier 20 member 2 (*SLC20A2*) (Wang *et al.*, 2012), xenotropic and polytropic retrovirus receptor 1 (*XPR1*) (Legati *et al.*, 2015), platelet-derived growth factor B (*PDGFB*) (Keller *et al.*, 2013), and platelet-derived growth factor receptor β (*PDGFRB*) (Nicolas *et al.*, 2013b). Recessively inherited PFBC is associated with mutations in myogenesis regulating glycosidase (*MYORG*) (Yao *et al.*, 2018). The estimated minimal prevalence is 4.5 per 10 000, suggesting that PFBC is not a rare disorder and is underdiagnosed (Nicolas *et al.*, 2018). The clinical penetration of PFBC is incomplete and heterogeneous comprising of psychiatric signs (e.g. anxiety, psychosis), cognitive impairment, migraine, and various movement disorders (e.g. ataxia, dystonia,

parkinsonism) (Manyam, 2005; Nicolas *et al.*, 2013b; Kasuga *et al.*, 2014). Histologically, the most striking feature of PFBC is the encrusted capillaries (Miklossy *et al.*, 2005), where calcifications cover vessels like 'pearls on a string'. The few available autopsy and case reports of patients with PFBC point to brain vascular insufficiency and blood–brain barrier damage (Gomez *et al.*, 1989; Miklossy *et al.*, 2005; Wszolek *et al.*, 2006; Wider *et al.*, 2009; Baker *et al.*, 2014; Kimura *et al.*, 2016). Although extensively calcified brain areas show neuronal preservation, neuronal pathology (e.g. Lewy bodies, neurofibrillary tangles or intracellular calcifications) has been described in PFBC cases (Miklossy *et al.*, 2005; Kimura *et al.*, 2016). PET studies on genetically confirmed familial and idiopathic cases of basal ganglia calcification have revealed presynaptic dopaminergic deficits in patients presenting with parkinsonism (Paschali *et al.*, 2009; Koyama *et al.*, 2017). Changes in glucose metabolism in non-calcified striatal and cortical areas have been described (Benke *et al.*, 2004; Le Ber *et al.*, 2007), indicating that calcifications could interfere with neuronal circuitry.

It is not known how mutations in *SLC20A2* and *XPR1*, which are a transmembrane inorganic phosphate (Pi) importer and exporter, respectively, *MYORG*, a putative glycosidase, and *PDGFB* and *PDGFRB*, a growth factor and receptor, respectively, lead to a common pathology. Several cell types at the neurovascular unit and in the brain parenchyma express these genes, and the contribution of each of these cell types for disease development is not known. Most of the described mutations in PFBC cases cause a loss-of-function of the protein (Wang *et al.*, 2012; Sanchez-Contreras *et al.*, 2014; Arts *et al.*, 2015; Legati *et al.*, 2015; Vanlandewijck *et al.*, 2015); however, some mutations may exert a dominant negative effect (Larsen *et al.*, 2017), or cause a cellular mislocalization of the protein (Taglia *et al.*, 2017). Accordingly, the molecular and cellular mechanisms leading to capillary calcification in PFBC may be multifactorial.

Ectopic soft tissue calcification is a common pathological feature of many diseases (Rashdan *et al.*, 2016; Nitschke and Rutsch, 2017) and although the primary cause is different, the subsequent formation of bone cells has been described in several calcification diseases. For example: in atherosclerosis, end-stage renal disease, and monogenetic

diseases such as generalized calcification of infancy, Hutchinson-Gilford progeria, the mineralization is thought to be driven by an active process resembling osteogenesis (Johnson *et al.*, 2006; Aikawa *et al.*, 2007; Toussaint *et al.*, 2009; Villa-Bellosta *et al.*, 2013; Leopold, 2015; Benz *et al.*, 2017). It is not known if vessel calcification in PFBC shares similarities with physiological bone formation. Hence, we addressed this question with a PFBC [*Pdgfb* hypomorph, *Pdgfb^{ret/ret}* (Keller *et al.*, 2013)] mouse model and genetically confirmed PFBC cases. We report that the cells surrounding calcified nodules express markers for osteoblasts, osteoclasts and osteocytes. In addition, we found that bone matrix proteins are deposited in calcifications and showed that this osteogenic environment accompanies a neurotoxic astrocyte response in *Pdgfb^{ret/ret}* mice. Of note, *Pdgfb^{ret/ret}* animals present specific behavioural and cognitive alterations, similar to those described in a subset of patients with PFBC.

Materials and methods

Mice

In this study, *Pdgfb^{ret/ret}* (*Pdgfb* hypomorphs) and *Pdgfb^{ret/wt}* (controls) mice of both genders were used (Lindblom *et al.*, 2003; Keller *et al.*, 2013). The mice were 2–4 months or 8–12 months of age. Experiments on mice were carried out in accordance to the protocols approved by the Cantonal Veterinary Office Zurich (permit numbers ZH196/2014, ZH067/2015, and ZH151/2017). The mice were housed under a 12-h light/dark cycle and were given food and water *ad libitum*.

Primary familial brain calcification patients

Genetically confirmed PFBC autopsy cases [*SLC20A2* genomic deletion (p.Met1_Val652del), *SLC20A2* p.Ser113*, *PDGFRB* p.(Arg695Cys)] were from Mayo Clinic Florida Brain Bank and have been described previously (Baker *et al.*, 2014; Sanchez-Contreras *et al.*, 2014). The study protocol on autopsy samples was approved by the Swiss Ethics Committee (Zürich, KEK-2018–00877).

Antibodies, peptides and bisphosphonates

Primary antibodies used for immunofluorescence staining are listed in Supplementary Table 1.

All fluorescently-labelled (Alexa 488, Cy3, DyLight 649) secondary antibodies made in donkey (anti-rabbit, anti-rat and anti-goat) suitable for multiple labelling were purchased from Jackson ImmunoResearch.

Peptide DSS₆ conjugated to 5(6)FAM [5(6)-carboxyfluorescein] was purchased from JPT Peptide Technologies. Bisphosphonates AF647-RISPC, 5(6)FAM-zolendronate and AF647-risedronate were purchased from Biovinc. The

250- μ m thick cleared brain slices were incubated overnight with the peptide DSS₆ or bisphosphonates, followed by a washing step with phosphate-buffered saline (PBS) and mounting in ProLong[®] Gold Antifade (Invitrogen).

Immunohistochemistry on mouse brain vibratome slices

Mice were deeply anaesthetized and transcardially perfused with ice-cold PBS followed by 4% paraformaldehyde (PFA), pH 7.2. Brains were removed and post-fixed 4–5 h in 4% PFA at 4°C. Mouse brains were sectioned with a vibratome (Leica VT1000S) into 60- μ m thick slices. Vibratome slices were blocked with 1% bovine serum albumin (BSA), 0.1% Triton[™] X-100 in PBS and incubated overnight at 4°C, followed by an incubation of 2 days with primary antibodies at 4°C. Slices were washed with 0.5% BSA, 0.05% Triton[™] X-100 in PBS and incubated overnight with secondary antibodies. Slices were stained with DAPI, followed by a final washing step in PBS, and mounted in ProLong[®] Gold Antifade (Invitrogen). Immunohistochemistry stains were imaged using a confocal microscope [Leica SP5, 20 \times NA (numerical aperture): 0.7, 63 \times NA: 1.4] or a stereomicroscope (Zeiss Axio Zoom.V16, 1 \times NA: 0.25). Images were analysed using the image-processing software Imaris (Bitplane). For stains that exhibited a salt-and-pepper noise, a median filter of 5 \times 5 \times 5 was applied to remove the noise. For all immunohistochemical studies, a minimum number of three animals was investigated per staining.

Quantification of calcifications and vessel density on brain serial sections

Brains were serially sectioned into 50- μ m thick slices using a vibratome (Leica VT1000S). Fifty-five sequential coronal sections were taken for immunohistochemistry, where the first section contained the posterior part of the commissura anteriori and the last section contained the posterior part of the hypothalamus and zona incerta. All vibratome sections were stained with antibodies against osteocalcin and collagen IV (Supplementary Table 1). Immunohistochemistry stains for the quantification of calcifications and vessel density were imaged using a confocal microscope (Leica SP5, 10 \times NA: 0.4). Images were acquired from the thalamic regions, consisting of two horizontal tiles from the left and right hemispheres. For quantification of calcifications, images were analysed using the image-processing software Imaris (Bitplane), where a surface for the osteocalcin staining (calcification channel) was created. Vessel density was quantified on 22 brain sections divided into right and left hemispheres from areas showing a high interindividual variation in calcification load. Vessels were identified using anti-collagen IV immunostaining and the vessel density was quantified in Fiji (Schindelin *et al.*, 2012) using vessel analysis plugin (version 1.1) with minor modifications. Prism7 software (GraphPad) was used to perform statistical analysis (one-way ANOVA, Pearson correlation test).

Immunohistochemistry on human brain sections

Paraffin-embedded brain sections were deparaffinized and hydrated. Antigen retrieval was performed using 0.01 M citrate buffer, pH 6.0 at 95°C. Tissue sections were blocked with 5% donkey serum, 0.2% TritonTM X-100 in PBS for 1 h at room temperature, followed by an overnight incubation with primary antibodies at 4°C. Tissue sections were washed with PBS and incubated for 2 h at room temperature with secondary antibodies. Nuclei were visualized using DAPI, followed by an incubation with filtered 0.3% Sudan black in 70% ethanol for 10 min. Slices were washed and mounted in ProLong[®] Gold Antifade (Invitrogen). Immunohistochemistry stains were imaged using a confocal microscope (Leica SP5, 20× NA: 0.7, 63× NA: 1.4). Images were analysed using the image-processing software Imaris (Bitplane).

Whole brain clearing, labelling of brain calcifications and SPIM imaging of calcifications

Mouse brain tissue for whole brain clearing was prepared according to a published protocol (Chung *et al.*, 2013), with minor modifications. Cleared brains were stained for 3 days at room temperature using 0.5 nmol of AF647-risedronate (Biovinc). The stained brains were washed in PBS and placed in refractive index matching solution [RIMS; 85% (w/v) Histodenz (Sigma)] for imaging. Brains were attached to a small weight and loaded into a quartz cuvette, then submerged in RIMS and imaged using a home-built mesoscale single-plane illumination microscope (SPIM), with a 1.25× zoom (field of view 10.79 mm; pixel size: 5.27 μm). Four fields of view were used to cover the whole mouse brain and were stitched in Fiji. The technical details of in house-built SPIM are described elsewhere (www.mesospin.org).

MRI

All MRI was performed on a 7T small animal MR Pharmascan (Bruker Biospin) equipped with an actively shielded gradient set of 760 mT/m with an 80 μs rise time and operated by a Paravision 6.0 software platform. Phase mapping and susceptibility-weighted imaging (SWI) was performed as described previously, with minor modifications (Klohs *et al.*, 2011). In brief, a circular polarized volume resonator was used for signal transmission and an actively decoupled mouse brain quadrature surface coil with integrated combiner and preamplifier was used for signal receiving (Bruker BioSpin). Mice were anaesthetized with an initial dose of 4% isoflurane (Abbott) in oxygen/air (200:800 ml/min) mixture and were maintained spontaneously breathing 1.5% isoflurane, supplied via a nose cone. Mice were placed on a water-heated support to keep body temperature within 36.5 ± 0.5°C, monitored with a rectal temperature probe. T₂*-weighted gradient-images were acquired with a flow-compensated Fast Low-Angle Shot (FLASH) gradient-echo sequence. Sequence parameters were echo time = 15 ms, repetition time = 350 ms, flip angle = 30, and number of averages = 16. Eleven horizontal slices of 0.5 mm thickness were recorded

with a field of view = 20 mm × 20 mm, an image matrix = 331 × 331 to give a spatial resolution = 60 μm × 60 μm. Fieldmap-based shimming was performed prior data acquisition using the automated MAPshim routine to improve the homogeneity of the magnetic field.

Image post-processing

Phase maps and susceptibility-weighted images were generated using Paravision software (Bruker). Data were processed in a standard fashion with a 2D Fourier transform to compute the magnitude images. A phase unwrapping Gaussian filter was used to remove slowly varying phase shifts. Phase masks were created by setting all positive phases to 1 and by scaling negative phases linearly between 0 and 1. These masks were multiplied four times with the corresponding magnitude image to create susceptibility-weighted images.

Quantification of calcifications on images generated using susceptibility-weighted imaging

Eleven SWI datasets were analysed. Serial images 4–10 containing calcification prone regions were selected for quantification. SWI images were compared with their phase image counterparts to ensure that the signal was due to a diamagnetic signal (i.e. presence of calcifications). SWI images were processed using Fiji (ImageJ) (Schindelin *et al.*, 2012), where images were contrast enhanced, thresholded and converted to a binary image. The area covered by calcifications in a region of interest in one SWI image was calculated from the obtained binary images. The region of interest used on serial SWI slices remained constant across the cohort analysed. Prism7 software (GraphPad) was used for statistical analysis (one-way ANOVA).

Behavioural studies

Adult mice (12 to 16 weeks) underwent behavioural testing. Testing began after 2 weeks of acclimatization in new holding room. Behavioural testing was carried out during the light phase in a dimly lit room. For all the tests except the light-dark box test and prepulse inhibition, a digital camera was mounted above the maze. Images were captured at a rate of 5 Hz and transmitted to a PC running the EthoVision tracking system (Noldus Information Technology, The Netherlands). For all behavioural experiments except for the light-dark box, two cohorts of mice were tested on separate occasions, where cohort I consisted of 18 mice (eight *Pdgfr^{ret/ret}*; 10 controls) and cohort II of 20 mice (10 *Pdgfr^{ret/ret}*; 10 controls). The number of animals used for each test is given in the respective figure legends.

Light-dark box

The light-dark box consisted of four identical two-way shuttle boxes (30 × 30 × 24 cm; Multi Conditioning System, TSE Systems). Boxes were separated by a dark Plexiglas[®] wall, and interconnected by an opening (3.5 × 10 cm) in the partition wall, thus allowing the animal to freely traverse from one compartment to another. This wall divided the compartment into a dark (1 lx) and a brightly illuminated (100 lx) compartment. Each mouse was placed in the centre of the dark

compartment and was allowed to move freely for 10 min. Innate anxiety (IA) was indexed as a per cent of time spent in the light compartment during 10 min of exploration:

$$IA = \left(\left[\frac{\text{time spent in light compartment}}{\text{total time}} \right] \times 100 \right) \quad (1)$$

Total distance moved was measured to ascertain that the per cent of time spent in the light compartment was not confounded by changes in locomotor activity.

Open field

The locomotor activity of mice was assessed in an open field set up, as described in detail elsewhere (Meyer *et al.*, 2005). The apparatus consisted of white Plexiglas® and was located in a testing room under diffuse lighting. A digital camera was mounted directly above the four arenas. Images were captured at a rate of 5 Hz and transmitted to a PC running the Ethovision (Noldus Information Technology, The Netherlands) tracking system. The mice were gently placed in a corner of the arena, and allowed to freely explore for 45 min, where the dependent measure (total distance moved) is expressed as a function of 5-min bins.

Prepulse inhibition

The set-up and analysis used was the same as described in (Weber-Stadlbauer *et al.*, 2017). For each of the three pulse intensities (100, 110, or 120 dBA) prepulse inhibition (PPI) was indexed as the percent of inhibition of the startle response detected in pulse-alone trials:

$$PPI = 100 \left(1 - \left[\frac{\text{mean reactivity on prepulse and pulse trials}}{\text{mean reactivity on pulse - alone trials}} \right] \right) \quad (2)$$

PPI was calculated for each animal, and for three prepulse intensities (+6, +12, or +18 dBA above background). One female *Pdgfb^{ret/ret}* mouse was excluded from the analysis as the calculated percentage of mean PPI was negative, indicating a lack of responsiveness from the individual mouse.

Social interaction

We assessed social interaction using a social approach test in a modified Y-maze as established before (Richetto *et al.*, 2017; Weber-Stadlbauer *et al.*, 2017). The per cent of time spent (TS) with the live mouse was calculated as follows:

$$TS = 100 \left(\frac{\text{time spent with the live mouse}}{\text{time spent with the live mouse} + \text{time spent with the dummy object}} \right) \quad (3)$$

This value was used to assess relative exploration time between a congenic mouse and an inanimate dummy object. Total distance moved was measured to ascertain that the per cent of time spent with the mouse was not confounded by changes in locomotor activity. One female *Pdgfb^{ret/ret}* mouse was excluded from the analysis since it did not explore all arms of the arena during the test.

Spontaneous alternation test

The apparatus was identical to the one described above for assessing social interaction. The apparatus was located in an experimental testing room under dim diffuse lighting. The apparatus was made of transparent Plexiglas and consisted of three identical arms (50 × 9 cm; length × width) surrounded

by 10-cm high transparent Plexiglas walls. The three arms radiated from a central triangle (8 cm on each side) and were spaced 120° from each other. The percentage of spontaneous alternation (SAT) was calculated as follows:

$$SAT = 100 \left[\frac{\text{number of alternations}}{\text{number of arm entries} - 2} \right] \quad (4)$$

Statistical analyses

Results are expressed as mean ± standard error of the mean (SEM). Following statistical tests were performed on Prism7 software (GraphPad): statistical analysis between two groups was assessed using a two-tailed *t*-test. Statistical analysis between multiple groups was assessed using one-way ANOVA with Tukey correction for multiple comparison. To assess for correlation between vessel density and calcification load, a Pearson correlation test was performed.

Behavioural studies

Dependent measures obtained in the SAT, the social interaction and the light/dark box test were analysed using 2 × 2 × 2 (genotype × gender × cohort) ANOVA. All dependent measures in the open field test were analysed using 2 × 2 × 2 (genotype × gender × cohort) ANOVA or using 2 × 2 × 2 × 9 (genotype × gender × cohort × bins) repeated measure-ANOVA. In the PPI test, the per cent of PPI was analysed using a 2 × 2 × 3 × 3 (genotype × gender × pulse level × prepulse level) repeated measures ANOVA. The reactivity to pulse-alone trials was analysed using a 2 × 2 × 3 (genotype × gender × pulse level) repeated measures ANOVA, and the reactivity to prepulse-alone trials using a 2 × 2 × 3 (genotype × gender × prepulse level) repeated measures ANOVA. Statistical significance was set at *P* < 0.05. All statistical analyses were performed using the statistical software StatView (SAS institute Inc.; version 5.0.1).

Data availability

The raw data that support the findings of this study are available from the corresponding author upon reasonable request.

Results

Ectopic calcifications in *Pdgfb^{ret/ret}* mice are confined to the brain

The clinical symptoms of PFBC are confined to the nervous system. However, microangiopathy in skin biopsies in *PDGFB*, *PDGFRB* and *XPR1* mutation carriers has been reported (Biancheri *et al.*, 2016; Nicolas *et al.*, 2017). Furthermore, *Slc20a2* deficiency leads to skeletal abnormalities (Dickinson *et al.*, 2016). Therefore, we investigated whether *Pdgfb^{ret/ret}* animals also exhibit abnormalities in the skeleton and present with soft tissue calcifications outside of the CNS using a micro-computed tomography (μCT). Control and *Pdgfb^{ret/ret}* animals were scanned, and 3D rendered μCT images were constructed. We could not detect any macroscopic differences in the skeleton of

control versus *Pdgfb^{ret/ret}* animals (Supplementary Fig. 1A). The extra-skeletal signal observed in the abdomen (Supplementary Fig. 1A) both in *Pdgfb^{ret/ret}* and control mice was confined to the gut (Supplementary Fig. 1B), thus this signal is likely due to the chow fed to the mice. Next, we investigated for ectopic calcification in the soft tissue, where we detected calcifications in the brain of *Pdgfb^{ret/ret}* animals, which is consistent with our previously published data (Keller *et al.*, 2013; Vanlandewijck *et al.*, 2015) (Supplementary Fig. 1C); however, we did not detect calcifications on large central and peripheral vessels, such as the aorta (Supplementary Fig. 1D) and the femoral artery (Supplementary Fig. 1E).

Although we did not detect soft tissue calcification outside the brain, we investigated nevertheless if *Pdgfb^{ret/ret}* animals show systemic disturbances that could lead or contribute to the vessel calcification in the brain. We applied a recently developed functional test (T_{50} test) (Pasch *et al.*, 2012) to determine the calcification propensity of sera of *Pdgfb^{ret/ret}* and control animals. This test estimates the efficiency of a serum's anti-calcification system to inhibit the formation of calcium phosphate nanocrystals and measures the time point of the transformation (T_{50}) of primary calciprotein particles (amorphous) to secondary calciprotein particles (crystalline) by challenging the tested serum with supersaturated calcium and phosphate solutions (Pasch *et al.*, 2012). No statistically significant difference in serum T_{50} values (i.e. calcification propensity) between *Pdgfb^{ret/ret}* and control animals was detected (Supplementary Fig. 1F). These data add additional evidence that serum's pro- and anti-calcifying factors are not imbalanced in PFBC and systemic alterations do not contribute to the pathogenesis of PFBC.

Interindividual variation in calcification load in *Pdgfb^{ret/ret}* animals

The presence of bilateral brain calcifications is the common denominator in all PFBC mutation carriers; however, the load of calcification shows a significant interindividual variation (Nicolas *et al.*, 2013b). To estimate the variation in calcification load between *Pdgfb^{ret/ret}* animals, we quantified calcifications *in vivo* in the deep regions of the brain using SWI and phase mapping. Both techniques use fully velocity compensated gradient-echo sequence data. The post-processing of the data reveals signal changes due to the presence of compounds that disturb the magnetic field, such as iron or calcium. In addition, filtered phase images allow the discrimination between diamagnetic (calcium) and paramagnetic (iron) compounds because they cause opposite phase shifts (Haacke, 2006). We acquired gradient-echo datasets from *Pdgfb^{ret/ret}* and control animals for SWI and phase post-processing, and reconstructed phase maps to determine the type of the compound causing magnetic field disturbances. Susceptibility-weighted images of *Pdgfb^{ret/ret}* animals showed hypointensities in calcification-prone regions

(Fig. 1A, yellow arrows) and the phase map analysis showed that these disturbances are due to calcium and not iron. No changes in tissue contrast were detected in images of control animals (Fig. 1A). Quantification of calcification load using susceptibility-weighted images revealed regional difference in calcification load between individual *Pdgfb^{ret/ret}* animals (Fig. 1B). In addition, the total calcification load quantification using susceptibility-weighted images, showed also a statistically significant difference between tested animals (Fig. 1C). Thus, the SWI and phase-analysis approach to determine the calcification load further confirmed the presence of calcium in vessel-associated lesions and demonstrated a regional, up to 3-fold, interindividual variation in the calcification load. These data show that despite of genetic homogeneity and controlled environment, calcification load in brains of *Pdgfb^{ret/ret}* animals is variable which is consistent with the calcification phenotype observed in human patients with PFBC.

Brain calcifications in *Pdgfb^{ret/ret}* mice bind bisphosphonates

Our current and previous analysis of vessel-associated calcifications in *Pdgfb^{ret/ret}* mouse brains demonstrated the presence of calcium and phosphate-containing lesions, which stained with histological bone stains [Supplementary Fig. 1A and C, see also Keller *et al.* (2013)]. We therefore extended the characterization of the bone-like consistency of vessel-associated calcifications by testing if these structures bind bisphosphonates. Bisphosphonates are chemical derivatives of pyrophosphate (PPi), which similarly to PPi, bind to calcium hydroxyapatite crystals in the bone with high affinity (Zhang *et al.*, 2007). We tested several fluorescently labelled bisphosphonates [AF647-RIS, AF647-RISPC, 5(6)-FAM-ZOL], which differ in their affinity to hydroxyapatite (Sun *et al.*, 2016). We observed that all bisphosphonates labelled brain calcifications although with different intensities. AF647-risedronate was selected to label calcifications in cleared whole brains of *Pdgfb^{ret/ret}* mice. Whole brain imaging further confirmed the localization of calcifications in the deep brain regions, occurring in a bilateral configuration (Fig. 1D and Supplementary Video 1), as described previously (Keller *et al.*, 2013). These data indicate the presence of hydroxyapatite, the crystalline form of calcium and phosphate present in bone and lend further support to the notion that vessel-associated nodules in *Pdgfb^{ret/ret}* mice have a bone-like consistency.

Bone matrix proteins are present in brain calcifications in *Pdgfb^{ret/ret}* mice

Having established that vessel-associated structures contain hydroxyapatite, we aimed to further characterize the extracellular matrix (ECM) composition of these and therefore stained brain tissue with antibodies recognizing bone ECM

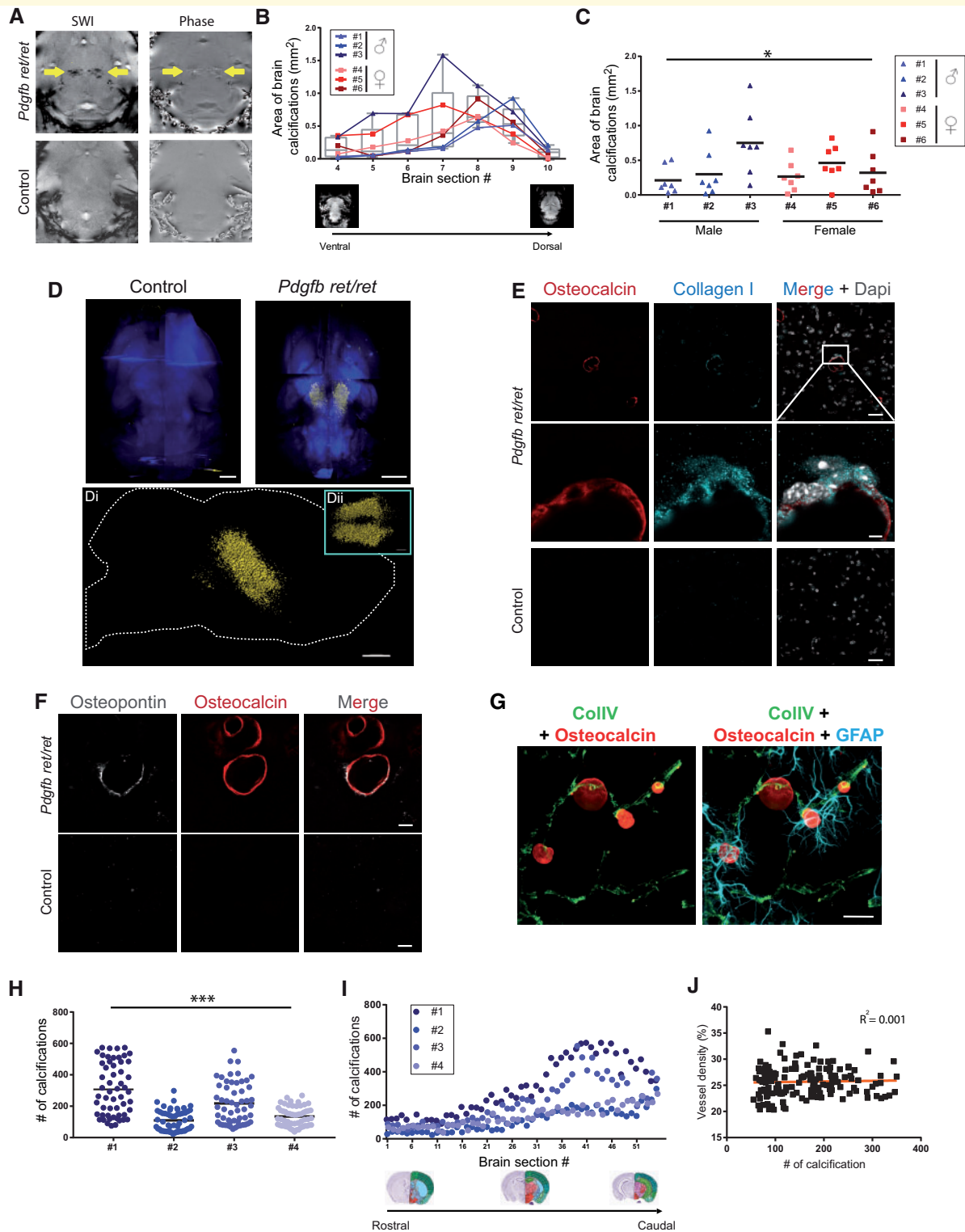


Figure 1 Interindividual variation in calcification load and osteoid-like consistency of brain calcifications in *Pdgfrb*^{ret/ret} animals.

(A) SWI sequence images and phase maps of the mouse brain. Calcifications (yellow arrows) were observed as black structures in the thalamic region on susceptibility-weighted images and as diamagnetic phase shifts on the corresponding phase maps. (B) Quantification of the calcification load in individual mice using susceptibility-weighted images, where calcification load is plotted against an individual imaged brain section (ventral to dorsal) and presented as box-plots indicating the mean and whiskers indicating minimum and maximum values, $n = 6$. (C) Quantification of calcification load using SWI analysis shows a significant difference between six individual *Pdgfrb*^{ret/ret} mice (one-way ANOVA; $P = 0.0284$). Bar indicates the mean. (D) Bisphosphonates (AF647-RIS, in yellow) stain brain calcifications in cleared whole brains of *Pdgfrb*^{ret/ret} animals. [D(i)] Sagittal view of a surface rendered image of the bisphosphonate staining. [D(ii)] Transverse view of bisphosphonate staining showing the bilateral distribution of brain calcifications. White dotted line delineates brain tissue. Scale bars = 3000 μm (D), 1000 μm [D(i)], 2000 μm [D(ii)]. (E) A

(continued)

components. Immunohistological analysis showed several bone matrix proteins in these brain lesions, such as collagen I (Fig. 1E), osteocalcin (Fig. 1E–G) and osteopontin (Fig. 1F). Co-staining with a blood vessel marker confirmed that aggregates positive for bone proteins are associated with vessels (Fig. 1G). Even though osteopontin and collagen I are abundant in bone, these proteins are expressed by many tissues other than bone. To the best of our knowledge, osteocalcin is secreted solely by osteoblasts (Gorski, 2011) and thus, the presence of osteocalcin indicates the presence of true bone forming cells in the brains of *Pdgfb^{ret/ret}* animals. Taken together, these results demonstrate that brain vessel-associated calcifications in *Pdgfb^{ret/ret}* mice have an osteoid consistency, containing collagen I, as well as non-collagenous bone proteins, such as osteopontin and osteocalcin.

The finding that calcifications can be labelled using antibodies against bone proteins gave us the opportunity to address whether the observed high variation in calcification load (Fig. 1B and C) is due to differences in vessel density among individual *Pdgfb^{ret/ret}* mice. Blood vessels and vessel-associated calcifications were visualized using immunohistochemistry and imaged using the laser scanning confocal microscope. We observed a high variance between individual mice in the total number of calcifications (Fig. 1H), where the calcification load differed regionally up to 3-fold (Fig. 1I), similar to calcification quantification data obtained using susceptibility weighting and phase mapping. We determined the vascular density in brain regions that showed the highest difference in calcification load. We did not observe a correlation between vessel density and calcification number ($R^2 = 0.001$; Fig. 1J) and, thus, differences in calcification number between different *Pdgfb^{ret/ret}* animals cannot be explained by differences in vessel density.

Osteoclast-like cells surround vessel-associated calcifications in *Pdgfb^{ret/ret}* mouse brains

The presence of osteocalcin in vessel-associated calcifications (Fig. 1E–G) prompted us to investigate if cells expressing bone cell markers (osteoclasts, osteoblasts and osteocytes) can be detected. Osteoclasts are multinucleated giant cells that express tartrate-resistant acid phosphatase

(TRAP), a widely used histochemical marker for osteoclasts (Boyle *et al.*, 2003). However, we were not able to observe multinucleated cells nor cells positive for TRAP enzymatic activity (not shown) around calcifications. We next investigated whether cathepsin K, a protease that is secreted by osteoclasts (Boyle *et al.*, 2003), can be detected around calcifications. We observed cathepsin K-positive cells around calcifications (Fig. 2A) and calcifications positive for this protease. The receptor activator of nuclear factor κ B (RANK)/RANK ligand (RANKL) signalling axis is important for bone remodelling, where osteoblasts express RANKL, which interacts with the receptor (RANK) expressed on the surface of osteoclasts, promoting osteoclast maturation (Boyle *et al.*, 2003). We observed RANK-positive cells surrounding calcified nodules (Fig. 2B). Altogether, we detected the expression of a subset of osteoclast markers by cells surrounding vessel-associated calcifications.

Osteoblast-like cells surround vessel-associated calcifications in *Pdgfb^{ret/ret}* mouse brains

Osteoblasts in bone express the transcription factor RUNX2, which is essential for skeletogenesis (Johnson *et al.*, 2006). In *Pdgfb^{ret/ret}* mouse brains, RUNX2-positive cells were found in close proximity to vessel-associated calcifications, where the localization of this transcription factor was nuclear (Fig. 2D), indicative of activation and transcriptional activity. We also detected RUNX2-positive cells in control animals in locations similar to those in *Pdgfb^{ret/ret}* mice. In contrast, RUNX2 was localized diffusely in the cytoplasm in control animals (Fig. 2D, yellow arrows). Another osteoblast marker, expressed by committed progenitors, is tissue non-specific alkaline phosphatase (ALPL) (Johnson *et al.*, 2006). ALPL staining revealed a zonated endothelial expression in both control and *Pdgfb^{ret/ret}* animals (Supplementary Fig. 2). In addition, we detected single, ALPL-positive cells that were negative for endothelial markers in calcification-prone regions in *Pdgfb^{ret/ret}* mice (Supplementary Fig. 2C), indicating the presence of osteoblast progenitors. To assess further if vessel-associated calcifications present an osteoblastic environment in *Pdgfb^{ret/ret}* animals, we stained brain sections

Figure 1 Continued

subset of osteocalcin-positive (in red) calcifications are positive for collagen I (in cyan). In addition, collagen I-positive cells are observed around calcifications. Nuclei are visualized using DAPI (in white). Scale bar = 30 μ m, magnified image = 4 μ m. (F) A subset of osteocalcin-positive (in red) calcifications are positive for osteopontin (in white). Scale bar = 10 μ m. (G). Osteocalcin-positive (in red) calcifications are vessel-associated (in green). Brain calcifications are surrounded by reactive astrocytes (in cyan). Scale bar = 20 μ m. (H) Quantification of calcification number using immunohistochemistry shows a significant difference between four individual *Pdgfb^{ret/ret}* mice (one-way ANOVA; $P = 0.0001$). Bar indicates the mean. (I) Number of calcifications increase on the rostral-caudal axis. X-axis shows the number of analysed brain slices. Illustrative brain sections indicate an approximate anatomical position of analysed brain sections (Image credit: Allen Institute). $n = 4$. (J) Vessel density is plotted against the calcification load in the brain regions which show variable calcification load (sections 43–55, see I) (Pearson correlation, $R^2 = 0.0012$). In total, 153 brain sections from four *Pdgfb^{ret/ret}* mice were analysed.

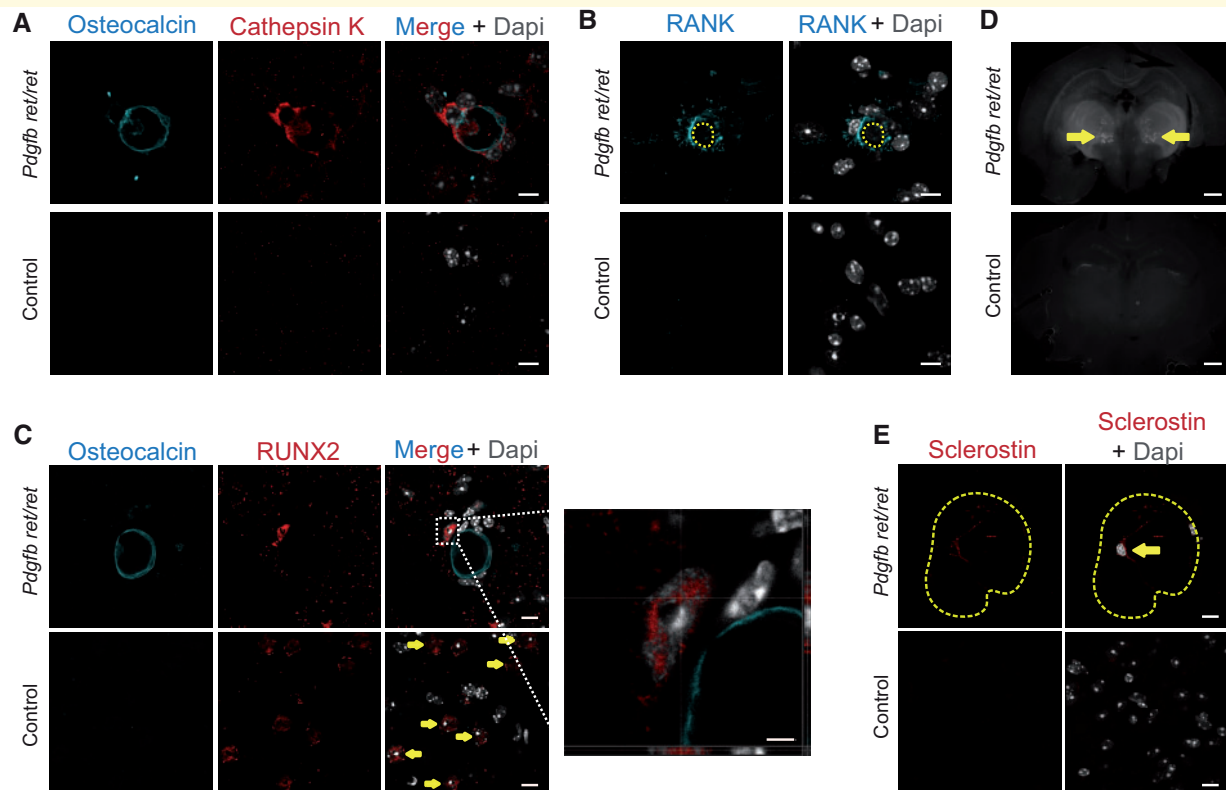


Figure 2 Presence of cells expressing osteoclast, osteoblast and osteocyte markers around calcifications in *Pdgfb^{ret/ret}* mouse brain. (A and B) Immunohistochemistry for osteoclast markers. (A) Cathepsin K-positive (in red) cells are observed in close vicinity to an osteocalcin-positive (in cyan) nodule. (B) RANK-positive cell (in cyan) around vessel-associated calcification (highlighted with yellow dotted line). (C) Staining of a cleared brain slice using a short peptide (DSS_6) (in white) specifically recognizing bone formation sites. Yellow arrows point to calcifications. (D) Immunohistochemistry for an osteoblast marker. RUNX2-positive (in red) cells are observed in proximity to osteocalcin-positive (in cyan) calcifications. Magnified orthogonal view of dotted area shows nuclear localization of RUNX2. Yellow arrows point to RUNX2-positive cells seen in control mice where the localization of RUNX2 is cytoplasmic. (E) Immunohistochemistry for an osteocyte marker sclerostin (in red). DAPI-positive (in white) cell located inside a sclerostin-positive (in red) calcification. Nuclei are visualized using DAPI (in white). Scale bars = 10 μm (A, B, D and E), 3 μm (magnified image, D), 1000 μm (C).

with a peptide $DSS_6-5(6)FAM$, which has been reported to bind specifically to osteoblastic sites in bone (Zhang *et al.*, 2012). Indeed, this peptide stained calcifications in cleared brains (Fig. 2C, yellow arrows) further confirming the presence of an osteoblastic environment of brain calcifications in *Pdgfb^{ret/ret}* animals.

Osteocyte-like cells reside within vessel-associated calcifications in *Pdgfb^{ret/ret}* mouse brains

In bone, osteoblasts become embedded in osteoid tissue and become osteocytes, stellate-shaped cells important for bone maintenance (Bonewald, 2011). Osteocytes express secreted glycoprotein sclerostin, a protein not expressed by other bone cells (Bonewald, 2011). Immunohistological detection of sclerostin revealed the presence of sclerostin immunopositivity in vessel-associated calcifications in *Pdgfb^{ret/ret}* animals (Fig. 2E). Furthermore, within sclerostin-positive

calcifications, we detected entrapped cell nuclei (Fig. 2E, yellow arrow) reminiscent of bone, where osteocytes reside within the bone structure (Bonewald, 2011). In addition, we stained for another osteocyte marker—the cell surface protein podoplanin (Wetterwald *et al.*, 1996)—but could not detect podoplanin reactivity within calcifications. Surprisingly, podoplanin was expressed by reactive astrocytes surrounding calcifications (Fig. 4A). Altogether, the presence of bone proteins, osteoclast-, osteoblast- and osteocyte-like cells at the site of vessel calcifications in brains of *Pdgfb^{ret/ret}* animals indicate the presence of an osteogenic environment.

Genetically confirmed PFBC cases exhibit an osteogenic environment around brain calcifications

Having established the presence of an osteogenic environment around vessel-associated calcifications in *Pdgfb^{ret/ret}*

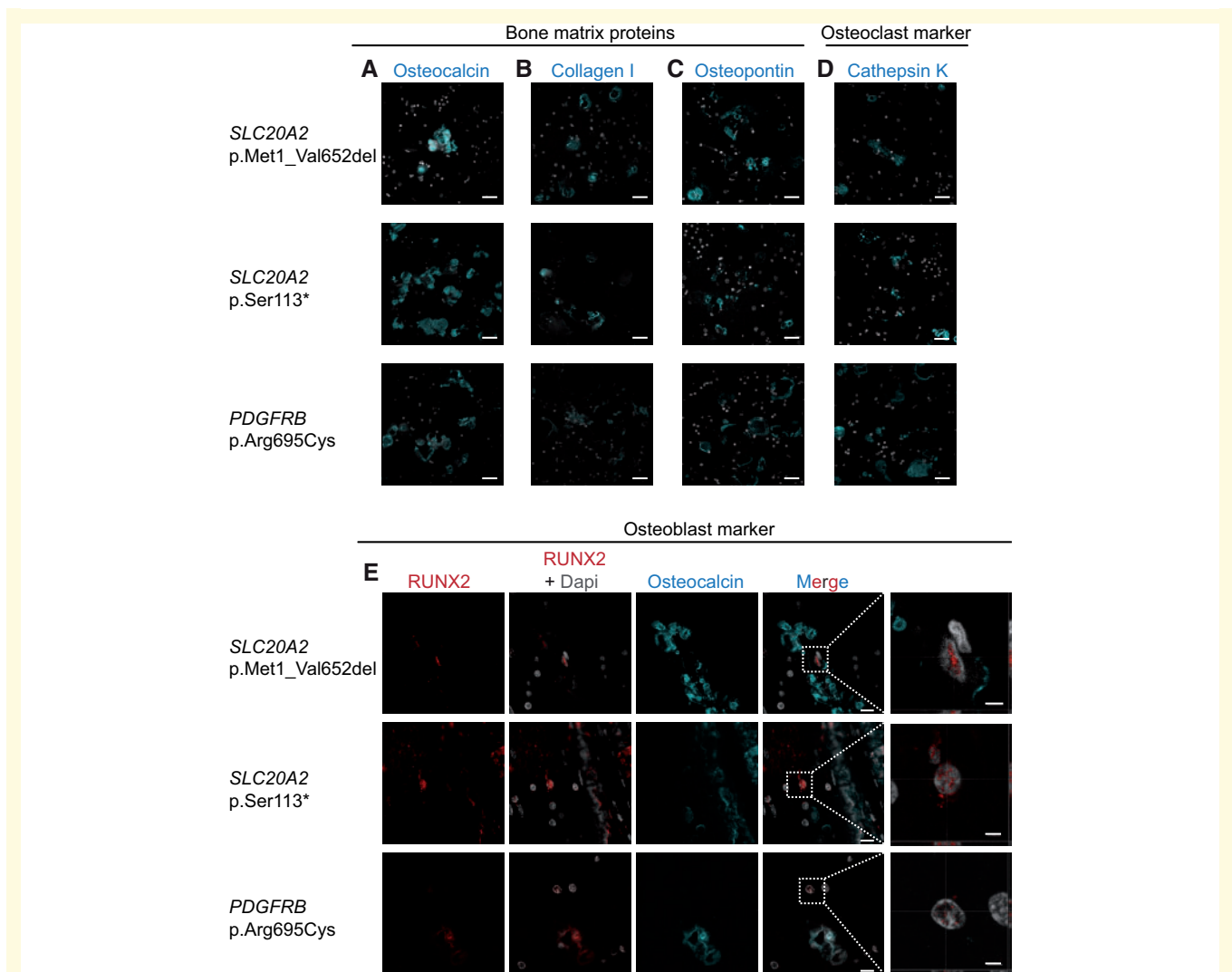


Figure 3 Presence of an osteogenic environment around brain calcifications in genetically confirmed PFBC. (A–C) Immunohistochemistry of bone matrix proteins (in cyan). Brain calcifications in PFBC cases stain for osteocalcin (A), collagen I (B), and osteopontin (C). (D) Immunohistochemistry for an osteoclast marker. Brain calcifications stain for cathepsin K (in cyan), a protein secreted by osteoclasts, indicating the presence of osteoclast-like cells. (E) Immunohistochemistry for an osteoblast marker. Cells in the vicinity of brain calcifications (in cyan) express RUNX2 (in red) localized to the nucleus. Nuclei are visualized using DAPI (in white, A–E). Magnified orthogonal views of dotted areas show nuclear localization of RUNX2. Scale bars = 30 μm (A–D), 10 μm (E), and 3 μm (magnified image, E).

animals, we wanted to evaluate the validity of these findings to human PFBC. Thus, we investigated if brain calcifications in the animal model exhibit a similar microenvironment as in genetically confirmed PFBC patients carrying mutations in *SLC20A2* (p.Met1_Val652del and p.Ser113*) or in *PDGFRB* (p.Arg695Cys). Similar to calcifications in *Pdgfr^{ret/ret}* brains, calcifications in PFBC brains showed the presence of osteocalcin, collagen I and osteopontin (Fig. 3A–C). We also observed the presence of cathepsin K, a protein secreted by osteoclasts, deposited in brain calcifications (Fig. 3D). Furthermore, we detected the nuclear localization of RUNX2, in cells in proximity to brain calcifications (Fig. 3E). These results demonstrate for the first time that brain vessel-associated calcifications

in PFBC patients have an osteoid consistency and are surrounded by an osteogenic environment. In addition, these data further affirm that the *Pdgfr^{ret/ret}* mouse model recapitulates pathological changes seen in PFBC cases.

Neurotoxic astrocytes surround vessel-associated calcifications

Our observation that reactive astrocytes surrounding calcifications express podoplanin (Fig. 4A) prompted us to explore the nature of reactive astrocytes surrounding calcifications. Brain regions void of calcifications in *Pdgfr^{ret/ret}* animals show normal distribution of microglia

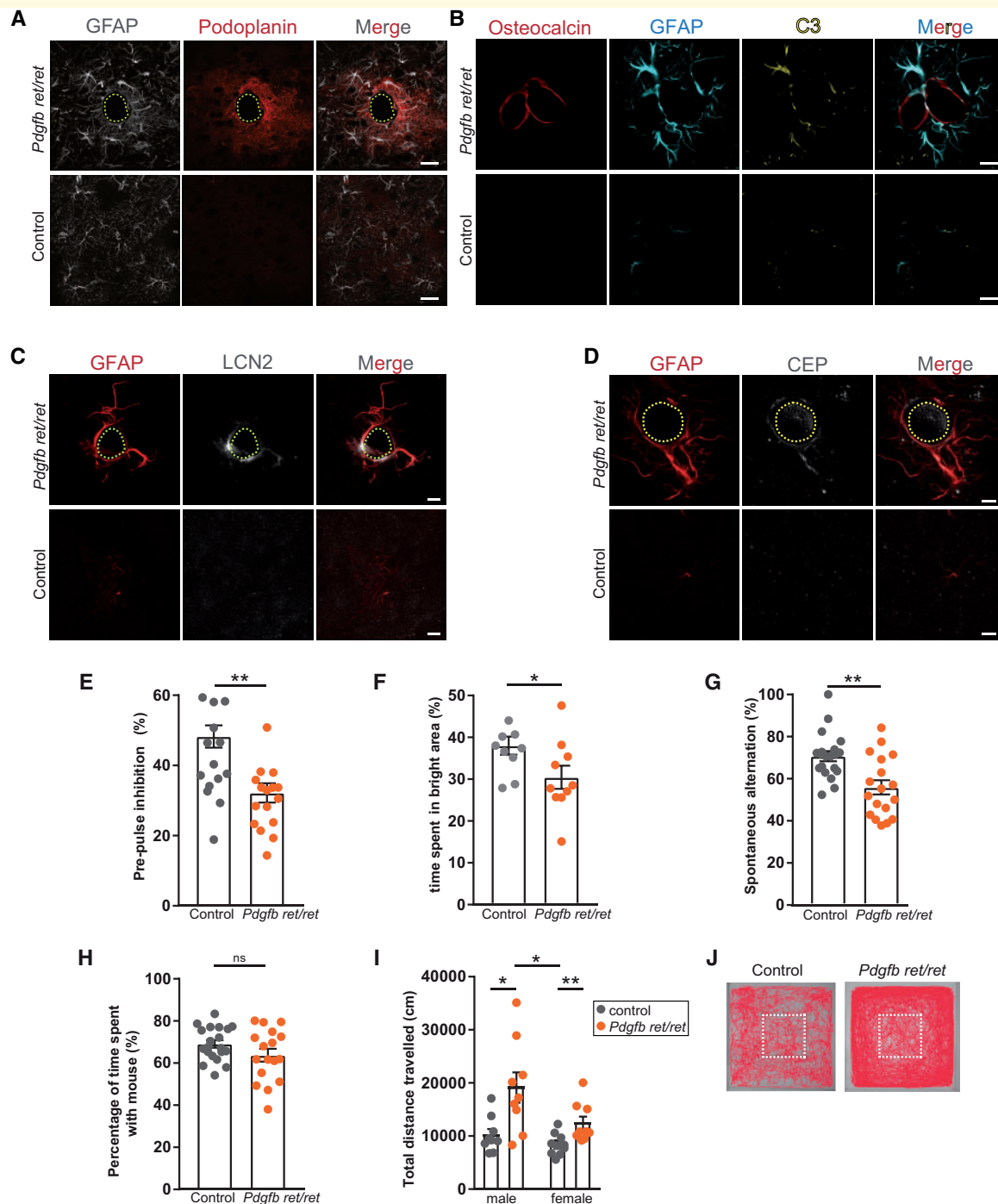


Figure 4 Neurotoxic astrocytes surround brain calcifications in *Pdgfb*^{ret/ret} animals and behavioral phenotype of *Pdgfb*^{ret/ret} animals. **(A)** Podoplanin is expressed by reactive astrocytes surrounding calcifications. GFAP-positive (in white) reactive astrocytes surrounding brain calcifications (marked with a yellow dotted circle) express podoplanin (in red). **(B)** marker for neurotoxic astrocytes, C3 (in yellow), co-localizes with GFAP staining (in cyan) around brain calcifications (in red) in *Pdgfb*^{ret/ret} mouse brains. **(C)** LCN2 (in white) co-localizes with GFAP staining (in red). **(D)** Carboxyethylpyrrole (CEP, in white) is found in GFAP-positive (in red) astrocytes around calcifications in *Pdgfb*^{ret/ret} mouse brain. Yellow dotted line in **A**, **C** and **D** mark calcifications. Scale bars = 30 μ m **(A)**, 15 μ m **(B)**, 10 μ m **(C)** and 8 μ m **(D)**. **(E–J)** Behavioural phenotype of *Pdgfb*^{ret/ret} animals. **(E)** PPI test, where the mean PPI is expressed as a percentage and calculated from the reflex outcome of a combination of three different prepulses and three different pulses ($P = 0.0005$); $n = 17–20$: 17 *Pdgfb*^{ret/ret}, 20 controls. **(F)** Light-dark box experiment, where the time spent in the bright area is expressed as a percentage of time during 10 min ($P = 0.039$); $n = 10$. **(G)** Spontaneous alternation test, where the alternations carried out by the mouse within 5 min are expressed as a percentage ($P = 0.0013$); $n = 18–20$: 18 *Pdgfb*^{ret/ret}, 20 controls. **(H)** Social interaction test, where the time spent with the unfamiliar mouse over the dummy during 5 min is expressed in percentage ($P = 0.241$); $n = 17–20$: 17 *Pdgfb*^{ret/ret}, 20 controls. **(I)** Open field test, where the total distance travelled by mice during 45 min is expressed in centimetres ($P = 0.0003$); $n = 18–20$: nine *Pdgfb*^{ret/ret} males, nine control males, nine *Pdgfb*^{ret/ret} females, 11 control females **(J)** Tracking illustration of the distance one mouse travelled during 45 min. White dotted box marks the centre zone. All data are means \pm SEM.

and astrocytes, but as shown previously, calcifications elicit a strong microglial and astrocyte response (Supplementary Fig. 3). Astroglialosis is a prominent feature of PFBC pathology, but little is known about specific changes in astrocytes. Recent studies show that astrocyte response to injury is heterogeneous and injury specific (Pekny and Pekna, 2016). However, the expression of recently described neurotoxic astrocyte (A1) markers is shared by different brain diseases (Liddel *et al.*, 2017). Thus, we tested whether reactive astrocytes surrounding calcifications express markers for A1 astrocytes. Figure 4B shows that GFAP-positive astrocytes surrounding calcifications express complement 3 (C3), a marker of neurotoxic astrocyte. To further confirm the neurotoxic response of astrocytes surrounding calcifications, we stained against lipocalin 2 (LCN2), a secreted protein by reactive astrocytes causing neuronal damage (Bi *et al.*, 2013). Also, LCN2 was expressed by GFAP-positive astrocytes surrounding calcifications (Fig. 4C). We also stained for 2- ω -carboxyethylpyrrole (CEP) adducts since increased phospholipid oxidation accompanies inflammation. Interestingly, we detected CEP immunoreactivity around calcifications, confined to GFAP-positive astrocytes (Fig. 4D). Thus, these results indicate that astrocytes surrounding calcifications in addition to a neurotoxic profile show signs of oxidative damage.

A subset of symptoms exhibited by PFBC patients is recapitulated in *Pdgfb^{ret/ret}* animals

Clinical symptoms in PFBC patients are variable and include cognitive, psychiatric and movement symptoms (Nicolas *et al.*, 2013b). To assess whether *Pdgfb^{ret/ret}* animals exhibit a behavioural phenotype, we performed a set of behavioural tests. We first assessed the sensorimotor gating by measuring the PPI of the acoustic startle reflex. This test measures the reduction in startle response to an acoustic stimulus (pulse), when the subject is exposed to a weak acoustic stimulus (prepulse) shortly beforehand (Supplementary Fig. 4A) (Hoffman and Searle, 1965). We found a striking main effect for genotype in the PPI, where *Pdgfb^{ret/ret}* mice presented a drastically decreased PPI (18%) compared to controls (Fig. 4E). Both, *Pdgfb^{ret/ret}* and control mice had comparable acoustic startle responses (Supplementary Fig. 4E) and their startle reflex was intensified with an increase in pre-pulse level (Supplementary Fig. 4F). We then evaluated the impact of genotype on innate anxiety-like behaviour using the light-dark box test. The light-dark box test is a widely used test to measure innate anxiety-like behaviour in rodents and is based on the natural aversion of mice to brightly illuminated areas as well as their spontaneous exploratory behaviour in novel environments (Supplementary Fig. 4B). *Pdgfb^{ret/ret}* mice displayed a significant decrease (~8%) in time spent in the bright area, signifying an increase in innate anxiety-

like behaviour compared to controls (Fig. 4F), which was not accompanied by changes in locomotor activity. Working memory was assessed by the spontaneous alternation test, which is based on the novelty preference of mice and measures the willingness of the tested animals to enter a new arm of the maze rather than returning to the previously visited arm (Supplementary Fig. 4C). In the spontaneous alternation test, *Pdgfb^{ret/ret}* mice exhibited a robust reduction in alternation (~13%) compared to controls (Fig. 4G). This observation indicates impaired spatial learning and memory in *Pdgfb^{ret/ret}* animals. In the social interaction test (Supplementary Fig. 4D), *Pdgfb^{ret/ret}* mice spent more time with the unfamiliar mouse (over 60%) than with the inanimate object, which was comparable to the behaviour of control mice (Fig. 4H). We also observed a significant main effect for the cohort in this test ($P = 0.0083$); however, this variable did not interact significantly with other dependent variables, i.e. gender or genotype (gender \times cohort, $P = 0.51$; genotype \times cohort, $P = 0.23$). This main effect is due to the general reduction in interaction with objects in the arena, i.e. unfamiliar mouse and dummy in the second tested cohort. The open field exploration test is a widely used behavioural assay to evaluate locomotor responses to novel environments in rodents. *Pdgfb^{ret/ret}* mice showed hyperactivity in the open field test (Fig. 4I and J) where the total distance moved was increased in *Pdgfb^{ret/ret}* animals. In addition, we observed a significant main effect between genders, where the total distance moved was increased in male *Pdgfb^{ret/ret}* mice compared to female *Pdgfb^{ret/ret}* mice (Fig. 4I). Interestingly, male *Pdgfb^{ret/ret}* mice increased in locomotion over time, unlike the other groups, where the locomotion decreased over time (Supplementary Fig. 4G). This overall increase in locomotion in *Pdgfb^{ret/ret}* animals resulted in an increase in centre zone entries (Supplementary Fig. 4H), but not in overall time spent in the centre zone (Supplementary Fig. 4I). Moreover, we did not observe a preferred spatial placement (Fig. 4J), suggesting that the movement of the mice was random and not subject to preference. Altogether, we found that *Pdgfb^{ret/ret}* animals exhibit sensorimotor gating deficits, hyperactivity, innate anxiety-like behaviour and reduced working memory, but unaffected social interaction.

Discussion

Our study provides a mechanistic insight into the pathophysiology of PFBC and implicates ossification as a cellular mechanism for the formation of vessel-associated calcifications. We also show that osteogenic environment elicits a neurotoxic astrocytic response, and that these pathologies are associated with behavioural changes in *Pdgfb^{ret/ret}* mice, a mouse model for PFBC. In addition, we demonstrate that tissue calcification in *Pdgfb^{ret/ret}* animals is confined to the CNS and is not caused by systemic alteration.

Bilateral microvascular calcification in the brain is a pathological hallmark of PFBC; however, the pathomechanism is not understood. In the current study, we confirm earlier findings and provide further evidence of the bone-like consistency of vessel-associated calcifications using a variety of imaging modalities (i.e. μ CT, MRI, fluorescent imaging) (Fig. 1, Supplementary Fig. 1 and Supplementary Video 1). Furthermore, we demonstrate that these bone-like structures are surrounded by cells expressing bone cell markers for osteoclasts and osteoblasts (Fig. 2 and Supplementary Fig. 2). Thus, the calcification of capillaries in PFBC is an active process mediated by osteoblast-like cells. The formation of bone-like cells often accompanies soft tissue calcification. The presence of these cells has been demonstrated around calcified lesions in atherosclerosis (Pugliese *et al.*, 2015), and in other genetic diseases of vessel calcification, such as generalized arterial calcifications of infancy (GACI) (Apschner *et al.*, 2014), pseudoxanthoma elasticum (PXE) (Hosen *et al.*, 2014), and in patients with chronic kidney disease (Nitschke and Rutsch, 2017). In addition, brain vessel calcification accompanies also other brain diseases, such as childhood developmental disorders (e.g. Sturge-Weber syndrome) (McCartney and Squier, 2014) and several neurodegenerative diseases (e.g. Alzheimer's disease, parkinsonism, diffuse neurofibrillary tangles with calcification), but little is known about the pathomechanism of vessel calcification in these diseases. Interestingly, in neurological disorders, it has been reported that non-collagenous bone matrix proteins (e.g. osteopontin, osteocalcin) are present in capillary-associated calcifications (Fujita *et al.*, 2003) pointing to similarities in protein content of calcifications with PFBC. Thus, vessel calcification in PFBC and other brain diseases could share common pathways with other ectopic calcification disorders presenting vessel calcification, regardless of the initial cause or anatomical location. This suggests that therapeutic approaches targeting vessel calcification in peripheral tissues could also potentially reduce brain calcification load in PFBC patients.

A recent study using *Slc20a2* heterozygous animals, a PFBC mouse model, did not find evidence of active deposition of mineralized calcium along the vessel wall (Wallingford *et al.*, 2017). Our data show that an osteogenic environment accompanies brain calcifications in PFBC irrespective of the causative mutation (Fig. 3). Thus, the lack of evidence of osteoblast-like cells around brain calcifications in *Slc20a2* heterozygous animals (Wallingford *et al.*, 2017) could be due to variation in the experimental procedures to detect bone cell markers around calcifications (e.g. tissue section thickness, tissue fixation, used antibodies).

In this study we have detected and quantified brain calcifications in *Pdgfb^{ret/ret}* animals using several *ex vivo* and *in vivo* approaches. We have used immunohistochemical detection on serial brain vibratome sections, bisphosphonate staining in cleared whole brains (both *ex vivo* analyses), and *in vivo* MRI using phase and SWI post-processing.

Quantification of the calcification load in the brains of *Pdgfb^{ret/ret}* animals using both *in vivo* and *ex vivo* methods have shown significant interindividual variation (Fig. 1). Of note, the high variation in calcification load occurs regionally. This interindividual variation of calcification load has been reported in human PFBC cases, but the clinical significance is not clear (Nicolas *et al.*, 2013b). Interindividual variation in calcification load was also recently reported in *Slc20a2*-deficient animals; however, no quantification of calcification load was performed (Jensen *et al.*, 2018). This and our data (Fig. 1) indicate that PFBC mutations are necessary for the formation of calcifications but the initiation frequency is stochastic. Additional factors other than a gene mutation contribute to the initiation and/or growth of vessel-associated calcifications. Thus, mouse models of PFBC show similarities in disease pathology, such as variation in calcification load and the time-dependent growth of calcifications (Keller *et al.*, 2013; Jensen *et al.*, 2018).

Several CNS pathologies show pathological features in peripheral tissues. For example, patients suffering from cerebral autosomal dominant arteriopathy with subcortical infarcts and leukoencephalopathy (CADASIL), caused by mutations in the *NOTCH3* gene, present with granular osmiophilic material within smooth muscle cells in brain and skin blood vessels (Chabriat *et al.*, 2009). A case study on PFBC individuals carrying *PDGFRB* and *XPR1* mutations reported microcalcifications in cutaneous vessels (Nicolas *et al.*, 2017); however, the pathological features were not identical to those observed in the brain. Nevertheless, we investigated whether *Pdgfb^{ret/ret}* mice present with calcifications in the peripheral tissues by using μ CT imaging. As previously reported (Keller *et al.*, 2013), we detected calcifications in the brain (Supplementary Fig. 1C) but not in other tissues. Further studies that address molecular, hemodynamic and biomechanical differences of vascular beds in various organs including brain (Jespersen and Ostergaard, 2012; Inden *et al.*, 2013) may provide clues to why patients with PFBC develop calcifications in certain brain regions.

In addition, we investigated whether systemic changes could lead to the development of local vessel calcification in the brain by using an *in vitro* test to measure the calcification propensity of serum (Pasch *et al.*, 2012). Although one of the diagnostic criteria for PFBC is the exclusion of altered serum concentrations of calcium, magnesium and phosphorus (Nicolas *et al.*, 2013b), the predisposition for calcium phosphate to precipitate can still be affected by altered levels of calcification-inhibiting factors (e.g. fetuin-A, albumin, magnesium, PPI). Lower levels of serum fetuin-A, a major systemic inhibitor of calcification, have been reported in patients with idiopathic bilateral basal ganglia calcifications (Demiryurek and Gundogdu, 2018). *Pdgfb^{ret/ret}* mice, similar to PFBC patients, do not present with altered calcium, Pi and magnesium levels in the serum when compared to control mice (Keller *et al.*, 2013) and results presented in this study show that there is no difference in serum calcification propensity between *Pdgfb^{ret/ret}* and control mice (Supplementary Fig. 1F).

Taken together, *Pdgfb^{ret/ret}* mice do not show alterations in the humoral anti-calcification defence and, thus, the formation of local vessel calcification in the brain in *Pdgfb^{ret/ret}* mice is not triggered by systemic alterations in the serum calcification propensity.

It is not yet fully known which cell types are the primarily affected cells in PFBC. Our previous studies have demonstrated that paracrine PDGF-BB signalling at the neurovascular unit protects from vessel calcification (Keller *et al.*, 2013), further highlighting the importance of neurovascular unit in disease pathogenesis. PFBC genes are expressed by different cell types at the neurovascular unit (i.e. endothelial cells, pericytes, astrocytes, microglia); however, a recent study demonstrated that *MYORG* is expressed only by astrocytes (Yao *et al.*, 2018). Thus, it is plausible that astrocyte dysfunction is a common denominator in PFBC pathophysiology. To this end, our study further points to the importance of astrocytes in PFBC. First, we show that astrocytes surrounding calcifications are positive for CEP adducts (Fig. 4D), which arise exclusively from the oxidation of docosahexaenoic (DHA)-containing lipids (Yakubenko and Byzova, 2017). The accumulation of CEP, a sign of oxidative damage, occurs in many diseases associated with chronic inflammation (e.g. atherosclerosis, macular degeneration) but also in autistic brain tissue (Evans, 2008; Yakubenko and Byzova, 2017). CEP modifications are strong triggers/catalysts of pathology by inducing pro-inflammatory response in macrophages (Yakubenko and Byzova, 2017). Thus, CEP modifications on reactive astrocytes surrounding calcifications in *Pdgfb^{ret/ret}* mice, in addition of indicating astrocytic oxidative stress around calcifications, might also contribute to the PFBC pathology by modifying an inflammatory response in calcification-associated microglia. Second, we show that vessel calcifications elicit a specific astrocytic response, which shares similarities with other neurodegenerative diseases. We found that astrocytes surrounding calcifications are positive for several proteins expressed in subsets of reactive astrocytes (podoplanin, C3, LCN2) (Fig. 4A–C). It has been shown that podoplanin is strongly expressed by a subset of reactive astrocytes in glioblastoma, and after ischaemic and stab wound injuries (Kolar *et al.*, 2015). Similarly, we detect a strong podoplanin expression in *Pdgfb^{ret/ret}* brains only in GFAP-positive astrocytes surrounding calcifications, confirming the presence of a subpopulation of astrocytes possessing a different activation profile. Additionally, we report that reactive astrocytes around brain calcifications express C3 (Fig. 4B). Recent studies have validated C3 as a marker for neurotoxic astrocytes (i.e. A1 type) in brain diseases (e.g. Alzheimer's, Parkinson's disease, multiple sclerosis) and in ageing (Liddelow *et al.*, 2017; Clarke *et al.*, 2018). Reactive astrocytes surrounding calcifications express also LCN2 (Fig. 4C), a biomarker for many inflammatory diseases, including atherosclerosis (Oberoi *et al.*, 2015). In the brain, the astrocyte-derived LCN2 has been shown to be toxic specifically for neurons (Bi *et al.*, 2013). Taken

together, these data pinpoint that astrocytes may play an important role in the pathophysiology of PFBC by potentially leading to neuronal damage and modifying inflammatory response.

The clinical manifestations of PFBC are heterogeneous (Nicolas *et al.*, 2013b). In addition, little is known about changes in neuronal networks leading to neuropsychiatric and motor deficits in PFBC. Case studies of few genetically confirmed PFBC patients presenting with parkinsonism point to presynaptic dopaminergic deficit (Paschali *et al.*, 2009; Koyama *et al.*, 2017). In this study, we have for the first time assessed whether a PFBC mouse model recapitulates some of the wide-range of neurological symptoms observed in PFBC patients. Behavioural testing comprised recognized readouts for innate anxiety, social interaction, locomotor activity, PPI and working memory. These tests were selected based on their relevance to the neurological symptoms observed in patients with PFBC. In addition, alterations in invariably calcified brain regions (i.e. basal ganglia) in patients with PFBC, as well as in animal models of PFBC, could modify the outcome of these tests. We report that *Pdgfb^{ret/ret}* mice present with increased anxiety and reduced cognition (Fig. 4F and G), but have no alterations in social interaction (Fig. 4H). In addition, *Pdgfb^{ret/ret}* mice also present with deficits in sensorimotor gating demonstrated by reduced PPI and hyperactivity (Fig. 4E, I and J). This behavioural phenotype recapitulates a subset of clinical symptoms (e.g. anxiety, psychosis, altered cognition) observed in PFBC patients (Nicolas *et al.*, 2013b). It is important to consider that mouse models of human brain disorders do not recapitulate the full spectrum of behavioural symptoms (Del Pino *et al.*, 2018). However, the behavioural alterations in *Pdgfb^{ret/ret}* mice are reproducible, which supports the validity of this animal model as an excellent translational research tool. Currently, it is not clear how capillary calcifications and/or the neurotoxic astrocytic response in the thalamus and midbrain in *Pdgfb^{ret/ret}* mice disturb the neural circuitry leading to these behavioural changes. However, PPI is executed and modulated by the functional connection between cortex and nuclei residing in calcification-prone brain regions (thalamic, midbrain) (Swerdlow *et al.*, 2001), where vessel calcifications could impair delivery of nutrients and oxygen into the neural tissue. Interestingly, a reduction in PPI and increased locomotion were reported in mice upon *Pdgfrb* deletion using *Nestin-Cre* (Nakamura *et al.*, 2015). The observed behavioural phenotype was attributed to the lack of *Pdgfrb* expression in neurons (Nguyen *et al.*, 2011). However, it should be noted that although nestin is a known neural stem cell marker, it is highly expressed by brain vascular cells, such as pericytes (Vanlandewijck *et al.*, 2018; Zeisel *et al.*, 2018), and by reactive astrocytes (Clarke *et al.*, 1994). Thus, deletion of *Pdgfrb* using *Nestin-Cre* could result in the knock-out of *Pdgfrb* in cell types other than neuronal progenitors. Nevertheless, it is intriguing that the ablation of *Pdgfrb* leads to similar behavioural

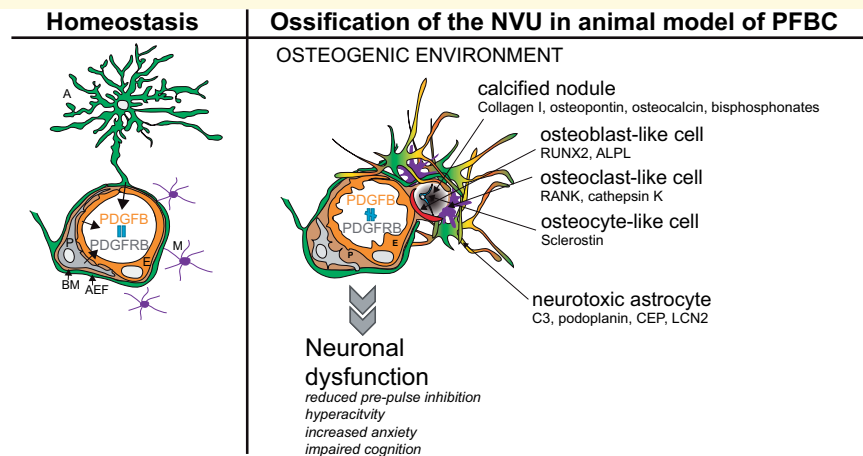


Figure 5 Alterations at the neurovascular unit accompanying vessel calcification in a mouse model of PFBC. Homeostasis: PDGFB/PDGFRB signalling at the neurovascular unit prevents vessel calcification. PDGFB is secreted by the endothelium and PDGFRB is expressed by mural cells and low level by astrocytes. Ossification of the neurovascular unit (NVU) in animal model of PFBC: altered PDGFB/PDGFRB signalling leads to the formation of bone cells (i.e. cells expressing osteoclast, osteoblast, osteocyte markers) and the deposition of structural bone proteins (e.g. collagen I, osteopontin, osteocalcin). Bone-like structures are closely surrounded by activated microglia and activated astrocytes. Astrocytes surrounding calcifications show signs of oxidative stress (i.e. CEP-positivity) and express markers for a subset of reactive astrocytes (LCN2, podoplanin), including the one for neurotoxic astrocytes (C3). Ossified vessels and neurotoxic astrocytic response is associated with neuronal dysfunction presenting in reduced PPI, hyperactivity, increased anxiety and impaired cognition. A = astrocyte; AEF = astrocyte endfeet; BM = basement membrane; E = endothelium; M = microglia; P = pericyte. Figure is modified from Betsholtz and Keller (2014).

phenotypes as PDGFB hypomorphism, which further corroborates the conclusion that disturbances in PDGFB/PDGFRB signalling axis in the CNS lead to an altered neuronal function.

Taken together, this study provides further insights into the pathogenesis of cerebrovascular calcifications in PFBC and the associated changes in neural tissue (Fig. 5). We show that vessel calcification is confined to the CNS and is accompanied by an osteogenic environment in *Pdgfb^{ret/ret}* mice. The latter findings were validated on autopsy material of genetically confirmed PFBC cases. We applied different methodologies to visualize and quantify brain calcifications and demonstrate that there is a significant inter-individual variation in calcification load. In addition, we show that vessel calcification elicits a neurotoxic astroglial response similar to those described in other neurodegenerative diseases. Ossification of the NVU and astrocyte changes are associated with behavioural alterations in *Pdgfb^{ret/ret}* mice, exhibiting deficits in the sensorimotor gating and cognition.

Although future studies using cell-type specific gene ablation of PFBC genes are needed to dissect the role of different cell types in PFBC aetiology, our study points to astrocytes as important players in the pathophysiology of PFBC. Future studies will be directed towards identification of pharmacologically targetable pathways that reverse vessel ossification and/or neurotoxic astrocytic response, and whether this leads to a reversal of behavioural phenotypes observed in *Pdgfb^{ret/ret}* mice.

Acknowledgements

The authors would like to thank Dr Elisabeth Rushing and Dr Susanne Wegener for discussions. Imaging was performed with equipment maintained by the Center for Microscopy and Image Analysis, University of Zurich.

Funding

This work was supported by the Swiss National Science Foundation (grant 31003A_159514), the Synapsis Foundation, Fonds zur Förderung des akademischen Nachwuchses (Zürich University), the Leducq Foundation (SphingoNet), the Swiss Heart Foundation to A.K., and Forschungskredit und Stiftung für Forschung an der Medizinischen Fakultät der Universität Zürich (grant FK-16-034) to Y.Z.

Competing interests

A.P. is an employee and stockholder of Calcicon AG, which commercializes the T50-Test.

Supplementary material

Supplementary material is available at *Brain* online.

References

- Aikawa E, Nahrendorf M, Figueiredo JL, Swirski FK, Shtatland T, Kohler RH, et al. Osteogenesis associates with inflammation in early-stage atherosclerosis evaluated by molecular imaging in vivo. *Circulation* 2007; 116: 2841–50.
- Apschner A, Huitema LF, Ponsioen B, Peterson-Maduro J, Schulte-Merker S. Zebrafish *enpp1* mutants exhibit pathological mineralization, mimicking features of generalized arterial calcification of infancy (GACI) and pseudoxanthoma elasticum (PXE). *Dis Model Mech* 2014; 7: 811–22.
- Arts FA, Velghe AI, Stevens M, Renaud JC, Essaghir A, Demoulin JB. Idiopathic basal ganglia calcification-associated PDGFRB mutations impair the receptor signalling. *J Cell Mol Med* 2015; 19: 239–48.
- Baker M, Strongosky AJ, Sanchez-Contreras MY, Yang S, Ferguson W, Calne DB, et al. SLC20A2 and THAP1 deletion in familial basal ganglia calcification with dystonia. *Neurogenetics* 2014; 15: 23–30.
- Benke T, Karner E, Seppi K, Delazer M, Marksteiner J, Donnemiller E. Subacute dementia and imaging correlates in a case of Fahr's disease. *J Neurol Neurosurg Psychiatry* 2004; 75: 1163–5.
- Benz K, Varga I, Neureiter D, Campean V, Daniel C, Heim C, et al. Vascular inflammation and media calcification are already present in early stages of chronic kidney disease. *Cardiovasc Pathol* 2017; 27: 57–67.
- Betsholtz C, Keller A. PDGF, pericytes and the pathogenesis of idiopathic basal ganglia calcification (IBGC). *Brain Pathol* 2014; 24: 387–95.
- Bi F, Huang C, Tong J, Qiu G, Huang B, Wu Q, et al. Reactive astrocytes secrete *lcn2* to promote neuron death. *Proc Natl Acad Sci U S A* 2013; 110: 4069–74.
- Biancheri R, Severino M, Robbiano A, Iacomino M, Del Sette M, Minetti C, et al. White matter involvement in a family with a novel PDGFB mutation. *Neurol Genet* 2016; 2: e77.
- Bonewald LF. The amazing osteocyte. *J Bone Miner Res* 2011; 26: 229–38.
- Boyle WJ, Simonet WS, Lacey DL. Osteoclast differentiation and activation. *Nature* 2003; 423: 337–42.
- Chabriat H, Joutel A, Dichgans M, Tournier-Lasserre E, Boussier MG. *Cadasil*. *Lancet Neurol* 2009; 8: 643–53.
- Chung K, Wallace J, Kim SY, Kalyanasundaram S, Andalman AS, Davidson TJ, et al. Structural and molecular interrogation of intact biological systems. *Nature* 2013; 497: 332–7.
- Clarke LE, Liddelaw SA, Chakraborty C, Munch AE, Heiman M, Barres BA. Normal aging induces A1-like astrocyte reactivity. *Proc Natl Acad Sci U S A* 2018; 115: E1896–905.
- Clarke SR, Shetty AK, Bradley JL, Turner DA. Reactive astrocytes express the embryonic intermediate neurofilament nestin. *Neuroreport* 1994; 5: 1885–8.
- Del Pino I, Rico B, Marin O. Neural circuit dysfunction in mouse models of neurodevelopmental disorders. *Curr Opin Neurobiol* 2018; 48: 174–82.
- Demiryurek BE, Gundogdu AA. Serum fetuin-A levels in patients with bilateral basal ganglia calcification. *Neurosci Lett* 2018; 666: 148–52.
- Deng H, Zheng W, Jankovic J. Genetics and molecular biology of brain calcification. *Ageing Res Rev* 2015; 22: 20–38.
- Dickinson ME, Flenniken AM, Ji X, Teboul L, Wong MD, White JK, et al. High-throughput discovery of novel developmental phenotypes. *Nature* 2016; 537: 508–14.
- Evans TA, Siedlak SL, Lu L, Fu X, Wang Z, McGinnis WR, et al. The autistic phenotype exhibits a remarkably localized modification of brain protein by products of free radical-induced lipid oxidation. *Am J Biochem Biotechnol* 2008; 4: 61–72.
- Forstl H, Krumm B, Eden S, Kohlmeyer K. Neurological disorders in 166 patients with basal ganglia calcification: a statistical evaluation. *J Neurol* 1992; 239: 36–8.
- Fujita D, Terada S, Ishizu H, Yokota O, Nakashima H, Ishihara T, et al. Immunohistochemical examination on intracranial calcification in neurodegenerative diseases. *Acta Neuropathol* 2003; 105: 259–64.
- Gomez CR, Luque A, Horenstein S. Microvasculopathy may precede idiopathic cerebral calcifications—case report. *Angiology* 1989; 40: 67–72.
- Gorski JP. Biom mineralization of bone: a fresh view of the roles of non-collagenous proteins. *Front Biosci (Landmark Ed)* 2011; 16: 2598–621.
- Haacke EM. Susceptibility weighted imaging (SWI). *Z Med Phys* 2006; 16: 237.
- Hoffman HS, Searle JL. Acoustic variables in the modification of startle reaction in the rat. *J Comp Physiol Psychol* 1965; 60: 53–8.
- Hosen MJ, Coucke PJ, Le Saux O, De Paepe A, Vanakker OM. Perturbation of specific pro-mineralizing signalling pathways in human and murine pseudoxanthoma elasticum. *Orphanet J Rare Dis* 2014; 9: 66.
- Inden M, Iriyama M, Takagi M, Kaneko M, Hozumi I. Localization of type-III sodium-dependent phosphate transporter 2 in the mouse brain. *Brain Res* 2013; 1531: 75–83.
- Jensen N, Schroder HD, Hejbol EK, Thomsen JS, Bruel A, Larsen FT, et al. Mice knocked out for the primary brain calcification-associated gene *Slc20a2* show unimpaired prenatal survival but retarded growth and nodules in the brain that grow and calcify over time. *Am J Pathol* 2018; 188: 1865–81.
- Jespersen SN, Ostergaard L. The roles of cerebral blood flow, capillary transit time heterogeneity, and oxygen tension in brain oxygenation and metabolism. *J Cereb Blood Flow Metab* 2012; 32: 264–77.
- Johnson RC, Leopold JA, Loscalzo J. Vascular calcification: pathobiological mechanisms and clinical implications. *Circ Res* 2006; 99: 1044–59.
- Kasuga K, Konno T, Saito K, Ishihara A, Nishizawa M, Ikeuchi T. A Japanese family with idiopathic basal ganglia calcification with novel SLC20A2 mutation presenting with late-onset hallucination and delusion. *J Neurol* 2014; 261: 242–4.
- Keller A, Westenberger A, Sobrido MJ, Garcia-Murias M, Domingo A, Sears RL, et al. Mutations in the gene encoding PDGF-B cause brain calcifications in humans and mice. *Nat Genet* 2013; 45: 1077–82.
- Kimura T, Miura T, Aoki K, Saito S, Hondo H, Konno T, et al. Familial idiopathic basal ganglia calcification: histopathologic features of an autopsied patient with an SLC20A2 mutation. *Neuropathology* 2016; 36: 365–71.
- Klohs J, Deistung A, Schweser F, Grandjean J, Dominietto M, Waschki C, et al. Detection of cerebral microbleeds with quantitative susceptibility mapping in the ArcAbeta mouse model of cerebral amyloidosis. *J Cereb Blood Flow Metab* 2011; 31: 2282–92.
- Kolar K, Freitas-Andrade M, Bechberger JF, Krishnan H, Goldberg GS, Naus CC, et al. Podoplanin: a marker for reactive gliosis in gliomas and brain injury. *J Neuropathol Exp Neurol* 2015; 74: 64–74.
- Koyama S, Sato H, Kobayashi R, Kawakatsu S, Kurimura M, Wada M, et al. Clinical and radiological diversity in genetically confirmed primary familial brain calcification. *Sci Rep* 2017; 7: 12046.
- Larsen FT, Jensen N, Autzen JK, Kongsfelt IB, Pedersen L. Primary brain calcification causal *Pit2* transport-knockout variants can exert dominant negative effects on wild-type *Pit2* transport function in mammalian cells. *J Mol Neurosci* 2017; 61: 215–20.
- Le Ber I, Marie RM, Chabot B, Lalevee C, Defer GL. Neuropsychological and 18FDG-PET studies in a family with idiopathic basal ganglia calcifications. *J Neurol Sci* 2007; 258: 115–22.
- Legati A, Giovannini D, Nicolas G, Lopez-Sanchez U, Quintans B, Oliveira JR, et al. Mutations in *XPR1* cause primary familial brain calcification associated with altered phosphate export. *Nat Genet* 2015; 47: 579–81.
- Leopold JA. Vascular calcification: mechanisms of vascular smooth muscle cell calcification. *Trends Cardiovasc Med* 2015; 25: 267–74.

- Liddelow SA, Guttenplan KA, Clarke LE, Bennett FC, Bohlen CJ, Schirmer L, et al. Neurotoxic reactive astrocytes are induced by activated microglia. *Nature* 2017; 541: 481–7.
- Lindblom P, Gerhardt H, Liebner S, Abramsson A, Enge M, Hellstrom M, et al. Endothelial PDGF-B retention is required for proper investment of pericytes in the microvessel wall. *Genes Dev* 2003; 17: 1835–40.
- Mann DM. Calcification of the basal ganglia in Down's syndrome and Alzheimer's disease. *Acta Neuropathol* 1988; 76: 595–8.
- Manyam BV. What is and what is not 'Fahr's disease'. *Parkinsonism Relat Disord* 2005; 11: 73–80.
- McCartney E, Squier W. Patterns and pathways of calcification in the developing brain. *Dev Med Child Neurol* 2014; 56: 1009–15.
- Meyer U, Feldon J, Schedlowski M, Yee BK. Towards an immunoprecipitated neurodevelopmental animal model of schizophrenia. *Neurosci Biobehav Rev* 2005; 29: 913–47.
- Miklossy J, Mackenzie IR, Dorovini-Zis K, Calne DB, Wszolek ZK, Klegeris A, et al. Severe vascular disturbance in a case of familial brain calcinosis. *Acta Neuropathol* 2005; 109: 643–53.
- Nakamura T, Matsumoto J, Takamura Y, Ishii Y, Sasahara M, Ono T, et al. Relationships among parvalbumin-immunoreactive neuron density, phase-locked gamma oscillations, and autistic/schizophrenic symptoms in PDGFR-beta knock-out and control mice. *PLoS One* 2015; 10: e0119258.
- Nguyen PT, Nakamura T, Hori E, Urakawa S, Uwano T, Zhao J, et al. Cognitive and socio-emotional deficits in platelet-derived growth factor receptor-beta gene knockout mice. *PLoS One* 2011; 6: e18004.
- Nicolas G, Charbonnier C, Campion D, Veltman JA. Estimation of minimal disease prevalence from population genomic data: application to primary familial brain calcification. *Am J Med Genet B Neuropsychiatr Genet* 2018; 177: 68–74.
- Nicolas G, Marguet F, Laquerriere A, Mendes de Oliveira JR, Hannequin D. Microangiopathy in primary familial brain calcification: evidence from skin biopsies. *Neurol Genet* 2017; 3: e134.
- Nicolas G, Pottier C, Charbonnier C, Guyant-Marechal L, Le Ber I, Pariente J, et al. Phenotypic spectrum of probable and genetically-confirmed idiopathic basal ganglia calcification. *Brain* 2013a; 136(Pt 11): 3395–407.
- Nicolas G, Pottier C, Maltete D, Coutant S, Rovelet-Lecrux A, Legallic S, et al. Mutation of the PDGFRB gene as a cause of idiopathic basal ganglia calcification. *Neurology* 2013b; 80: 181–7.
- Nitschke Y, Rutsch F. Inherited arterial calcification syndromes: etiologies and treatment concepts. *Curr Osteoporos Rep* 2017; 15: 255–70.
- Norman RM, Urich H. The influence of a vascular factor on the distribution of symmetrical cerebral calcifications. *J Neurol Neurosurg Psychiatry* 1960; 23: 142–7.
- Oberoi R, Bogalle EP, Matthes LA, Schuett H, Koch AK, Grote K, et al. Lipocalin (LCN) 2 mediates pro-atherosclerotic processes and is elevated in patients with coronary artery disease. *PLoS One* 2015; 10: e0137924.
- Pasch A, Farese S, Graber S, Wald J, Richtering W, Floege J, et al. Nanoparticle-based test measures overall propensity for calcification in serum. *J Am Soc Nephrol* 2012; 23: 1744–52.
- Paschali A, Lakiotis V, Messinis L, Markaki E, Constantoyannis C, Ellul J, et al. Dopamine transporter SPECT/CT and perfusion brain SPECT imaging in idiopathic basal ganglia calcinosis. *Clin Nucl Med* 2009; 34: 421–3.
- Pekny M, Pekna M. Reactive gliosis in the pathogenesis of CNS diseases. *Biochim Biophys Acta* 2016; 1862: 483–91.
- Pugliese G, Iacobini C, Blasetti Fantauzzi C, Menini S. The dark and bright side of atherosclerotic calcification. *Atherosclerosis* 2015; 238: 220–30.
- Puvanendran K, Low CH, Boey HK, Tan KP. Basal ganglia calcification on computer tomographic scan. A clinical and radiological correlation. *Acta Neurol Scand* 1982; 66: 309–15.
- Rashdan NA, Rutsch F, Kempf H, Varadi A, Leftheriotis G, MacRae VE. New perspectives on rare connective tissue calcifying diseases. *Curr Opin Pharmacol* 2016; 28: 14–23.
- Richetto J, Massart R, Weber-Stadlbauer U, Szyf M, Riva MA, Meyer U. Genome-wide DNA methylation changes in a mouse model of infection-mediated neurodevelopmental disorders. *Biol Psychiatry* 2017; 81: 265–76.
- Sanchez-Contreras M, Baker MC, Finch NA, Nicholson A, Wojtas A, Wszolek ZK, et al. Genetic screening and functional characterization of PDGFRB mutations associated with basal ganglia calcification of unknown etiology. *Hum Mutat* 2014; 35: 964–71.
- Schindelin J, Arganda-Carreras I, Frise E, Kaynig V, Longair M, Pietzsch T, et al. Fiji: an open-source platform for biological-image analysis. *Nat Methods* 2012; 9: 676–82.
- Sun S, Blazewska KM, Kadina AP, Kashemirov BA, Duan X, Triffitt JT, et al. Fluorescent bisphosphonate and carboxyphosphonate probes: a versatile imaging toolkit for applications in bone biology and biomedicine. *Bioconjug Chem* 2016; 27: 329–40.
- Swerdlow NR, Geyer MA, Braff DL. Neural circuit regulation of prepulse inhibition of startle in the rat: current knowledge and future challenges. *Psychopharmacology (Berl)* 2001; 156: 194–215.
- Taglia I, Formichi P, Battisti C, Peppoloni G, Barghigiani M, Tessa A, et al. Primary familial brain calcification with a novel SLC20A2 mutation: Analysis of PiT-2 expression and localization. *J Cell Physiol* 2017; 233: 2324–31.
- Toussaint ND, Elder GJ, Kerr PG. Bisphosphonates in chronic kidney disease; balancing potential benefits and adverse effects on bone and soft tissue. *Clin J Am Soc Nephrol* 2009; 4: 221–33.
- Vanlandewijck M, He L, Mae MA, Andrae J, Ando K, Del Gaudio F, et al. A molecular atlas of cell types and zonation in the brain vasculature. *Nature* 2018; 554: 475–80.
- Vanlandewijck M, Lebouvier T, Andaloussi Mae M, Nahar K, Hornemann S, Kenkel D, et al. Functional characterization of germline mutations in PDGFB and PDGFRB in primary familial brain calcification. *PLoS One* 2015; 10: e0143407.
- Vermersch P, Leys D, Pruvo JP, Clarisse J, Petit H. Parkinson's disease and basal ganglia calcifications: prevalence and clinico-radiological correlations. *Clin Neurol Neurosurg* 1992; 94: 213–17.
- Villa-Bellosta R, Rivera-Torres J, Osorio FG, Acin-Perez R, Enriquez JA, Lopez-Otin C, et al. Defective extracellular pyrophosphate metabolism promotes vascular calcification in a mouse model of Hutchinson-Gilford progeria syndrome that is ameliorated on pyrophosphate treatment. *Circulation* 2013; 127: 2442–51.
- Volpi S, Picco P, Caorsi R, Candotti F, Gattorno M. Type I interferonopathies in pediatric rheumatology. *Pediatr Rheumatol Online J* 2016; 14: 35.
- Wallingford MC, Chia JJ, Leaf EM, Borgeia S, Chavkin NW, Sawangmake C, et al. SLC20A2 deficiency in mice leads to elevated phosphate levels in cerebrospinal fluid and glymphatic pathway-associated arteriolar calcification, and recapitulates human idiopathic basal ganglia calcification. *Brain Pathol* 2017; 27: 64–76.
- Wang C, Li Y, Shi L, Ren J, Patti M, Wang T, et al. Mutations in SLC20A2 link familial idiopathic basal ganglia calcification with phosphate homeostasis. *Nat Genet* 2012; 44: 254–6.
- Weber-Stadlbauer U, Richetto J, Labouesse MA, Bohacek J, Mansuy IM, Meyer U. Transgenerational transmission and modification of pathological traits induced by prenatal immune activation. *Mol Psychiatry* 2017; 22: 102–12.
- Wetterwald A, Hoffstetter W, Cecchini MG, Lanske B, Wagner C, Fleisch H, et al. Characterization and cloning of the E11 antigen, a marker expressed by rat osteoblasts and osteocytes. *Bone* 1996; 18: 125–32.
- Wider C, Dickson DW, Schweitzer KJ, Broderick DF, Wszolek ZK. Familial idiopathic basal ganglia calcification: a challenging clinical-pathological correlation. *J Neurol* 2009; 256: 839–42.

- Wszolek ZK, Baba Y, Mackenzie IR, Uitti RJ, Strongosky AJ, Broderick DF, et al. Autosomal dominant dystonia-plus with cerebral calcifications. *Neurology* 2006; 67: 620–5.
- Yakubenko VP, Byzova TV. Biological and pathophysiological roles of end-products of DHA oxidation. *Biochim Biophys Acta* 2017; 1862: 407–15.
- Yao XP, Cheng X, Wang C, Zhao M, Guo XX, Su HZ, et al. Biallelic mutations in MYORG cause autosomal recessive primary familial brain calcification. *Neuron* 2018; 98: 1116–23.
- Zeisel A, Hochgerner H, Lonnerberg P, Johnsson A, Memic F, van der Zwan J, et al. Molecular architecture of the mouse nervous system. *Cell* 2018; 174: 999–1014.e22.
- Zhang G, Guo B, Wu H, Tang T, Zhang BT, Zheng L, et al. A delivery system targeting bone formation surfaces to facilitate RNAi-based anabolic therapy. *Nat Med* 2012; 18: 307–14.
- Zhang S, Gangal G, Uludag H. ‘Magic bullets’ for bone diseases: progress in rational design of bone-seeking medicinal agents. *Chem Soc Rev* 2007; 36: 507–31.
- Zhu D, Mackenzie NC, Farquharson C, Macrae VE. Mechanisms and clinical consequences of vascular calcification. *Front Endocrinol (Lausanne)* 2012; 3: 95.